



Remaining Fatigue Life Assessment of Plasma Sprayed Thermal Barrier Coatings

Philippe Robin, François Gitzhofer, Pierre Fauchais, and Maher Boulos

(Submitted September 15, 2009; in revised form February 18, 2010)

Ceramic functional coatings are frequently applied to structural materials, covering a wide range of thermomechanical and electrochemical applications. The main limiting feature is their reliability when subjected to cyclic transient thermal stresses. The study described in this article is a continuation of earlier research study focused on acoustic emission (AE) monitoring of the thermomechanical aging effects in ceramic coatings. Here, emphasis is placed on the usefulness of combining AE short-term monitoring with finite element modeling (FEM) to predict the performance of such coatings when subjected to cyclic thermal loads. The FEM study presented in this article is based on a three-dimensional, time-dependent approach, of the stress fields that developed within the coatings during the post-deposition cooling step and the thermal cycling. Experiments were conducted using yttrium-stabilized zirconia (YSZ) and Alumina (Al_2O_3) ceramic coatings combined with a NiCr-based intermetallic bond coat.

Keywords acoustic emission, alumina, finite element modeling, thermal barrier coating (TBC), thermal cycling, yttrium-stabilized zirconia (YSZ)

1. Introduction

Oxide ceramic materials commonly show specific properties of relatively high hardness, high passive resistance to chemical and thermo-chemical aggressions, and low thermal conductivity. Therefore, oxide ceramics are widely used as protective coatings applied to various underlying alloys. Among them, thermal barrier coatings (TBCs) applied to the hot sections of gas turbines, aero-engines, or diesel engines, are extensively used. TBCs are generally subjected to cyclic thermal shocks, which mainly consist in a transient thermal stress, resulting from a transient thermal gradient, applied to the material. In general, the worst conditions develop during engine cooling, either when the power is reduced or the engine is shut down. Since most coated components are cooled from their backside during operation of the engine, a thermal gradient applies previously to any transient conditions (Ref 1). A recent study, through presenting the delaminating mechanisms in coatings that experience thermal

gradients, has shown that delaminating within the oxide layer can be explained by the presence of significant stress gradient within the coating. It has also been shown in this article that both transient and equilibrium temperatures play a key role in the fracture mechanics (Ref 2).

Acoustic emission (AE) monitoring of TBC under thermal and thermal cycling conditions has already been investigated in the literature. Berndt et al. exposed that the AE count rate can be connected to the microstructural modifications of ceramic coatings as well as to the residual stress within the coating (Ref 3). It has also been demonstrated that AE signals of high amplitude can be associated with macro-cracking whereas signals of average and weak amplitude can be connected with micro-cracking (Ref 4). Another study, based on thermally sprayed ceramic coatings, pointed out that coatings without bond coat have emitted fewer signals during the first cycles than those with a bond coat, while after several cycles they have emitted more (Ref 5). During the first cycles, if the coating without bond coat has emitted less AE, then one could draw the conclusion that the remaining life is larger for coatings without bond coat, which is not in agreement with experiments. Therefore, it seems that a minimum number of fatigue cycles are needed before relating with confidence the AE count to the thermomechanical aging of the coating. Then, the point is how the number of cycles to be achieved can be quantified before a short-term AE monitoring can be considered as reliable to be used for remaining life assessment. In other words, what appears here is that, if crack lengths are not known before the first cyclic test, then it is hazardous to derive any conclusion about the remaining fatigue life, i.e., life under sub-critical crack growth conditions, using AE monitoring. Thus, the aim of the model is to confront the numeric results with the actual AE behavior of the coupons during a short-term AE monitoring to set up a reliable procedure. The long-term monitoring of the AE behavior for these

Philippe Robin, Centro de Nanociencias y Nanotecnología (CNYN), Universidad Nacional Autónoma de México, Ensenada, Mexico; **François Gitzhofer**, Centre de Recherche en Energie Plasma et Electrochimie (CREPE), Université de Sherbrooke, Sherbrooke, Canada; **Pierre Fauchais**, Sciences des Procédés Céramiques et Traitements de Surface (SPCTS), Université de Limoges, Limoges, France; and **Maher Boulos**, Tekna Plasma Systems Inc., Sherbrooke, Canada. Contact e-mail: philippe.c.robin@usherbrooke.ca and maher.boulos@Tekna.com.

specific samples has already been presented in the literature (Ref 6).

The computations were conducted using a dedicated finite element code, named CASTEM, developed by the Council of Atomic Energy (CEA, France). The code allowed using a three-dimensional (3D) approach, time resolved together with nonlinear computation of temperature fields, under various thermal loading conditions. The modeling of the deposition's residual stress has been previously presented in the literature by different authors (Ref 7, 8). Nevertheless, in those studies, the whole coating has been assumed to be stress free at the deposition temperature, i.e., during spraying. In that way, the coefficient of thermal expansion (CTE) mismatch is considered to be the main parameter triggering the stress both during the after-deposition cooling step and during the thermal cycling test. For each time step, the thermal fields are calculated, leading to the computation of the associated stress fields, using the Hooke's law extended to thermo-elastic behavior. No plasticity is taken into account since the duration of the heating period is 160 s, and the plastic deformation is known to be a weak source of AE (Ref 9). The computed thermal stresses do not take into account any pre-existing cracks or any remaining stress built-up during the spraying. It is proposed here to associate the stress, computed under ideal material conditions as soon as the spraying step finishes, to the short-term AE monitoring. Precisely, the AE behavior during the first cycle of the ceramic coatings with and without bond coat has to be well explained before presenting any remaining life prediction procedure based on short-term AE monitoring. The latter point will represent the topic of this study.

In order to assess the potentiality of using AE monitoring on a short-term range during a given thermal shock, actual materials and architecture of the samples have been chosen trying to make a relevant case. Two ceramic materials have thus been considered, alumina (Al_2O_3) and yttrium-stabilized zirconia (YSZ), the latter applied both with and without a (NiCr)6Al-based bond coat. On the one hand, alumina is known to be poorly resistant to thermal shocks but it does provide a good resistance to wear and erosion at high temperatures. The crystallographic structure of the as sprayed alumina has been reported in the literature to be predominantly the metastable $\gamma\text{-Al}_2\text{O}_3$ phase (Ref 10, 11). During heat treatment, phase transformation from $\gamma\text{-Al}_2\text{O}_3$ to $\alpha\text{-Al}_2\text{O}_3$, with the transition phases $\delta\text{-Al}_2\text{O}_3$ and $\theta\text{-Al}_2\text{O}_3$ created in between, has also been reported (Ref 12, 13). It can be assumed with reasonable confidence that phase transformations will take place during spraying and any thermal cycling tests conducted over 1000 °C. On the other hand, YSZ is well known to provide a good resistance to thermal shocks and, therefore, is successfully used in various states of the art plasma sprayed coatings for high temperature engines applications. Thus, YSZ has been applied on the substrate with and without bond coat, while alumina has been only sprayed on a bond coat. In those studies, duplex samples composed of a bond coat and a ceramic top coat are referred to as TBC, i.e., TBC- Al_2O_3 , and TBC-YSZ,

while without bond coat only the name of the sprayed material is used, i.e., YSZ. The finite element analysis will be focused on the YSZ and TBC-YSZ samples, since ceramic material and spraying conditions are identical, and the resulting phase is stabilized. Nevertheless, the short-term AE monitoring will concern the all the three samples.

2. AE and Cyclic Fatigue Life

In the case of thermally sprayed coatings, the resulting coating's microstructure is composed of several overlapping, layered, and micro-cracked splats, maintained together by interlocking structural forces. The construction of such coatings with the resulting quenching stress has been explained by the Kuroda and Clyne model (Ref 14). Impacting YSZ particles are rapidly quenched with very high cooling rates in the order of 10^6 to 10^9 K s^{-1} upon particle impact (Ref 15). The release of most of the quenching stress developed in each ceramic splat upon impact is induced by the micro-cracking phenomenon. That is why, only the CTE mismatch is usually considered to be the main parameter responsible of the stress state within the coating under thermomechanical load. During cyclic fatigue conditions, the failure process is considered to arise through a sequence of cracks nucleation, propagation, and coalescence events. If sufficiently high stresses are present within the coating, then cracks initiate and propagate leading to the final degradation of the system. The damage accumulation starts as soon as the molten particles impact the substrate during the deposition process.

Liu et al. have already proposed a phenomenological life prediction model for TBCs under repetitive thermal shocks based on the general fatigue life model of Basquin (Ref 16). Using Finite Element Modeling (FEM), it has been shown that this model is accurate within a factor of 3, i.e., three times the standard deviation. The Basquin equation representing the finite life of a material in terms of cyclic fatigue can be expressed by Eq 1.

$$N_f = A(\Delta\sigma)^m \quad (\text{Eq 1})$$

where N_f is the TBC spalling life in cycles, A and m are the constants that are to be fitted to life data collected from the thermal shock tests, and $\Delta\sigma$ is the cyclic stress range. Thus, the phenomenological damage variable considered in that model is the maximum stress that will apply during fatigue tests. The Basquin's approach to fatigue resistant design is, therefore, based on the drawing-up of the S-N curves, also known as Wöhler curves (Ref 17, 18). Moreover, the stress-based approach does not provide any indication about the rate at which already existing cracks are likely to develop. Therefore, it cannot be used with accuracy to assess the severity of pre-existing cracks and the remaining fatigue life of a given structure (Ref 19). Paris and Erdogan proposed the range of stress intensity factor (ΔK) as the characteristic parameter for fatigue tests (Ref 20, 21). During fatigue,

the crack growth rate can be described by the Paris-Erdogan equation (Eq 2).

$$\frac{da}{dN} = C(\Delta K)^n \quad (\text{Eq 2})$$

where the da/dN is the subcritical cyclic crack growth, C and n are the material parameters, and ΔK is the stress intensity factor range. A simple model for ΔK is given by

$$\Delta K = B \Delta S (\pi \cdot a)^{1/2} \quad (\text{Eq 3})$$

where B is a material parameter, ΔS the stress range, and a the crack length.

It has already been shown experimentally in the literature that AE count rates show reasonable correlation with crack propagation rates in steel and welded steel structures (Ref 22). Moreover, in the case of steel railroad bridges a relationship between AE count rate and fatigue crack growth has already been proposed by Gong et al. using a similar power law, Eq 4 (Ref 23).

$$\frac{d\eta}{dN} = C(\Delta K)^p \quad (\text{Eq 4})$$

where $d\eta/dN$ is the cyclic AE count rate, C and p are the material parameters, and ΔK remains the stress intensity factor range. Therefore, this last equation provides a natural link between nondestructive AE monitoring and qualitative fracture mechanic methods for predicting the rate of cracks propagation. Based on this model, where the AE count rate is related to the stress factor range ΔS and the instantaneous crack length, it may be possible to predict the remaining service life of damaged structures from the results of a short-term AE monitoring.

3. Experimental Details

Actual test samples are beam-shaped AISI 304SS substrates $370 \times 25.4 \times 1.4 \text{ mm}^3$. The general aspect of the actual test sample is shown in Fig. 1. Coatings are sprayed over an area of $120 \times 25.4 \text{ mm}$, centered on the substrate,

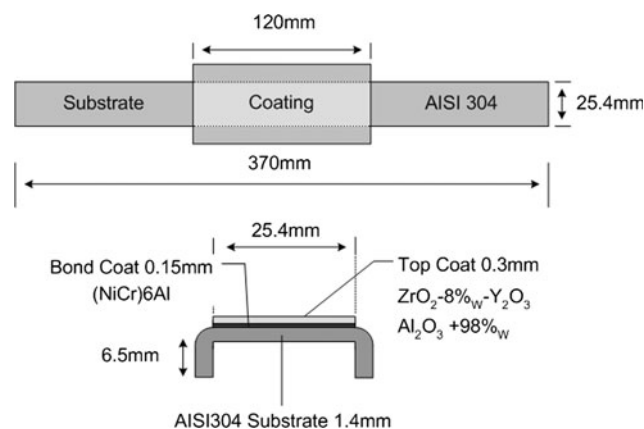


Fig. 1 General aspect of the coated samples

in order to fit closely to the furnace's length. Ceramic and metallic powders were obtained from Sulzer Metco (Sulzer Metco, Winterthur, Switzerland). The (NiCr)6Al bond coat powder size is $-125 + 45 \mu\text{m}$. The YSZ $\text{ZrO}_2\text{-Y}_2\text{O}_3$ ceramic powder size is $-75 + 45 \mu\text{m}$ while that of the alumina (Al_2O_3) is $-45 + 15 \mu\text{m}$. Samples' deposition was performed using a TEKNA AS-103L (Sherbrooke, Canada) direct current plasma torch. The bond coat thickness, if applied, is of $150 \mu\text{m}$, while the ceramic coatings are $300 \mu\text{m}$ thick. Spray parameters are detailed in Table 1. During spraying, the samples are air-cooled from the upper surface, i.e., the last deposited layer, during the rotation of the substrates which is set at 120 rpm. In order to avoid any residual warping of samples during both deposition and cycling steps, a mechanical reinforcement is obtained by folding the substrate plate below the deposited area before deposition. Since YSZ is applied using the same spray parameters in both cases, i.e., with or without bond coat, it can reasonably be supposed that they exhibit quite close material properties at the end of the spraying step.

During the heating periods, an air flow of 1 slpm was injected parallel to the sample, as shown in Fig. 2(b). This was done to simulate the real cooling system conditions encountered inside a turbine and maintain a thermal gradient through the sample. In that application, folding the plate helps also in confining the air stream along the substrate back surface.

Table 1 Spray parameters of the coating materials (injector i.d. is of 1 mm, anode nozzle i.d. is of 5 mm)

Parameters	Bond coat	Zirconia	Alumina
Primary gas (Ar), slpm	45	45	45
Secondary gas (H_2), slpm	15	15	15
Powder feed rate, g/min	20	15	10
Carrier gas (Ar), slpm	2.7	2.2	1.8
Power, kW	37	37	37
Arc current, A	500	500	500
Stand-off distance, mm	100	100	80

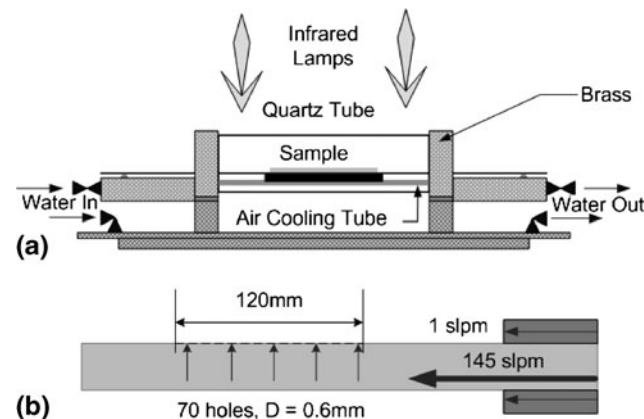


Fig. 2 Schematic side view of the experimental thermal shock test rig (a) and air cooling tube mounting details (b)

In Fig. 2(a), a side view of the experimental thermal shock test rig that has been developed to reproduce the thermal shock conditions encountered inside a turbine combustion chamber can be seen. Two kilowatts halogen lamps, focused on the coating area, were used as the furnace heat source. The radiative incident heat flux was measured using a radiant flux meter adapted to the harsh environment and positioned in the place of the sample. The measured flux was $145 \pm 9 \text{ kW/m}^2$. Samples were inserted into a quartz tube to isolate the system from potential external fluctuations. Thermal cycles consisted of a 160-s heating period at the full power of the infrared lamps, followed by a 180-s cooling period, with the lamps shut down. During the cooling periods, samples were cooled from the back surface by an air stream of 145 slpm, injected perpendicularly onto the sample through some 70 holes, focused on the deposition area, as shown in Fig. 2(b). The coating surface and the substrate's rear surface temperatures were measured, using two K thermocouples specially mounted for this purpose, onto the center of the corresponding surfaces. Two additional thermocouples were used to measure the ambient temperature inside the tube. One was positioned between the cooling tube and the sample, while the other was placed between the side of the sample and the quartz tube. The sample's surface temperature reaches values up to 1331 K during the heating period. The maximum rear side recorded temperature was 978 K. The parallel 1 slpm airflow maintained the realistic temperature gradient of about 350° . At the end of the cooling period, the sample's temperature fell to an approximately homogenous 329 K. Therefore, this operation provided a reproducible 1000 K thermal shock. The total duration of the cycle was about 340 s.

4. Finite Element Modeling

Only the part of the substrate that bears the coating, and the coating itself, are modeled. The meshing of samples appears to be a three superposed plate's assemblage, i.e., substrate, bond coat, and top coat. Conventionally, plates have been analyzed in two dimensions by treating them as surface elements that can take into account the plate thickness. Nevertheless, plate elements do not have provision for the calculation of the normal forces across the layers while brick elements have. Thus, the parabolic 20-node hexahedron element has been chosen since it permits the computation of the normal and shear stress distributions and their variations throughout the material thickness. In order to achieve calculations, the coupons discretization is made up of 4650 elements and 24500 nodes. According to the solid brick element specifications, each node has three spatial degrees of freedom plus one additional degree of freedom for temperature. This raises the system's degree of freedom up to a total of 98000. Boundaries' conditions are applied to the model to reproduce the conditions encountered by the sample during thermal cycling inside the bench. Since neither

plasticity nor cracks are modeled, the study is focused on the thermal modeling. In order to describe post-deposition cooling step and the thermal cycle, several thermal loadings are applied. The chosen resolution procedure enables a nonlinear thermal problem, with free and forced convection, conduction, and radiation, associated with time steps to be carried out. In the model, the Neumann's condition was chosen (imposed heat flux). Therefore, heat-transfer coefficients were calculated for all the sides of the meshing.

For the post-deposition cooling step, four thermal loadings, i.e., heat-transfer coefficients, are used. In the case of thermal cycle modeling, eight are necessary to take into account the thermal loads that occur during the heating and cooling steps. Ambient temperature is set at 293 K. The during-deposition temperature is 723 K, as measured by means of heat-sensitive enamels applied to the back faces of samples. The different heat-transfer coefficients were calculated for every 25° interval. The thermal loadings experienced during the post-deposition cooling step, i.e., heat-transfer coefficients, which are applied to the six faces of the sample were calculated using the empirical relationships found in the literature (Ref 24). In the case of the thermal cycle modeling, the free convection coefficients were calculated while taking into account two monitored temperatures inside the quartz tube during an actual test run, i.e., upper quartz tube air temperature and back face air temperature. A parallel-to-the-substrate airflow of 1 slpm is maintained during heating periods, which induces a different ambient temperature for the backside than for the rest of the sample. The re-emitted radiation corresponding heat-transfer coefficients were calculated, using a procedure from the Castem code, and separately for the upper and lower faces. The incident flux was measured experimentally and is also an entry parameter. All heat-transfer coefficients for free convection were calculated twice, i.e., for both the heating period and the cooling period, using the same either increasing or decreasing 25° step mode of calculation. The data tables so obtained were inserted as entry parameters into the model.

The determination of the heat-transfer coefficient for the forced convection that is applied to the back face of the sample during cooling is also a parameter that needs to be calculated. The temperature of the cooling air jet is 293 K. Since it is hard to estimate the stagnation zone value to be used in the forced convection heat-transfer calculation, considering the actual system, a slot of equivalent width replaces the row of nozzles in the calculation. The slot's width is adjusted to provide the same gas flow rate and velocity as the row of nozzles, for the same length. Reynolds and Nusselt numbers are calculated using the empirical relationship for a single slot, as found in the literature (Ref 24). The forced convection heat-transfer coefficient found using this method was equal to $260 \text{ W/m}^2 \text{ K}$. In the model, Young's and Poisson's modules are not temperature dependent, while the coefficients of thermal expansion, conductivity, and emissivity are. Thermal and mechanical properties of materials involved in the model are all taken from the literature and

Table 2 Thermomechanical properties of coating materials used in the finite element model

Properties	YSZ	Bond coat	Substrate
Emissivity	0.907-0.656	...	0.1043-0.2042
Thermal conductivity, $W m^{-1} K^{-1}$	1.52-1.68	14.6-34.3	14-36
Specific heat, $J kg^{-1} K^{-1}$	49.951-644.138	271.7-919.6	376.2-489.06
Thermal expansion, $10^{-6} K^{-1}$	6.5-11.6	11.6-21.2	14.7-21.4
Poisson coefficient	0.26	0.31	0.29
Young modulus, Pa	2×10^{10}	1.1×10^{11}	2.2×10^{11}
Mass density, $kg m^{-3}$	5500	7150	7900

displayed in Table 2 (Ref 1, 25-28). Because of the micro-cracked structure of the ceramic coating, the values of Young's modulus obtained by ultrasonic methods, which take into account the inherent differences between compressive and tensile measurements performed on cracked samples, were considered more reliable (Ref 29). Meshing convergence, model sensitivity to material properties, and time convergence have been presented elsewhere (Ref 30, 31).

5. Numeric Results

In the following time-resolved evolution curves, values are extracted from two points through the thickness, Z axis, chosen in the centre of the sample's faces. Consequently, these points are situated at the mid-width, Y axis, and the mid-length, X axis, of the meshing. This position is considered as the furthest from the plate's limits. The stress values in the study will refer to a computed stress corresponding to a discreet time within the studied step. Stress range, ΔS , will refer to the actual stress increment, relatively to a previously applied stress state.

5.1 Post-Deposition Cooling Step

No temperature recordings for the transient cooling phenomena of samples measured immediately after deposition were obtained. However, the total cooling time, necessary to reach room temperature was readily measured, as 20 min. In Fig. 3 and 4, the time-resolved development of the normal in-plane stresses, called S_{XX} and S_{YY} , located at the ceramic/metal interface can be seen, Fig. 3(a) and 4(a), and the ceramic's surface in Fig. 3(b) and 4(b). The computed cooling rate is also displayed in these figures. The time step in the post-deposition step modeling is 10 s. Results for both TBC-YSZ and YSZ samples are presented.

It can be seen from these figures that the cooling times to reach 298 K is 17 min. Calculation shows that the cooling rate values during the first 30 s, ranging from $-55 K s^{-1}$ at 10 s to $-15 K s^{-1}$ at 30 s, correspond to those of the post-deposition thermal down shocks. Cooling

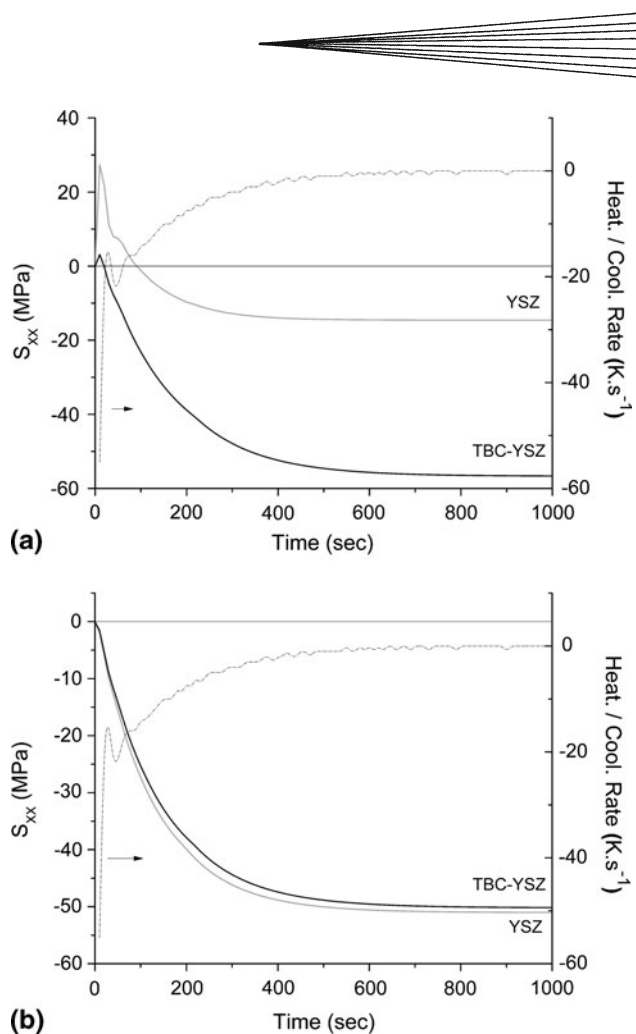


Fig. 3 Time-resolved in-plane normal stresses S_{XX} profiles for TBC-YSZ and YSZ samples, during the post-deposition cooling step extracted from the metal/ceramic interface (a) and the ceramic's surface (b)

rates are extracted from the center of the upper surface of the ceramic layer. Between 30 and 40 s, a second variation of the cooling rates is noted. This variation shows the equalization of temperatures within the plate. After 1000 s, the cooling rates of both faces are equal to zero. The radial thermal gradient through the plate's thickness is also equal to zero with a corresponding homogeneous temperature equal to ambient. The post-deposition cooling step has, therefore, been achieved, and any occurred transient tensile stress has contributed to the thermal aging of the samples. The stress values at the interface, observed in Fig. 3(a) and 4(a), are attributed to the CTE mismatch between the layers and the substrate, since the upper part of the ceramic layer stays globally under compressive stress. It is assumed that the thermal gradient throughout the upper part of the ceramic layer is not sufficient to involve surface quenching stress, as it can be seen in Fig. 3(b) and 4(b). Thus, as a first remark about the model's results, the analysis of the stress fields within the ceramic layer can be simplified by creating two specific zones, the metal/ceramic interface, which is always

subjected to the CTE mismatch, and the upper part of the ceramic layer, more subjected to the transient thermal gradient.

At the interface, in the case of YSZ, the CTE mismatch induces stress values up to 28 MPa for S_{XX} and 34 MPa for S_{YY} . At the interface, in the case of TBC-YSZ sample, the values are quite lower, in the order of 3 MPa for S_{XX} and 8 MPa for S_{YY} . Thus, at the end of the post-deposition cooling step, the stress range that has developed at the interface of the YSZ sample during the first seconds is several times higher than in the case of TBC-YSZ. From that result, it can be assumed that the degradation states of the two samples are different; the thermal aging in the case of YSZ sample being more advanced which can affect the AE behavior during at least the first cycles of the test. As a reminder, these results do not take into account any stress subsequent to the grit blasting operation before spraying or subsequent to the spraying process. They may not represent the entirely the stress state of the samples but are needed to assess the thermal stress ranges that may trigger further acoustic emissions.

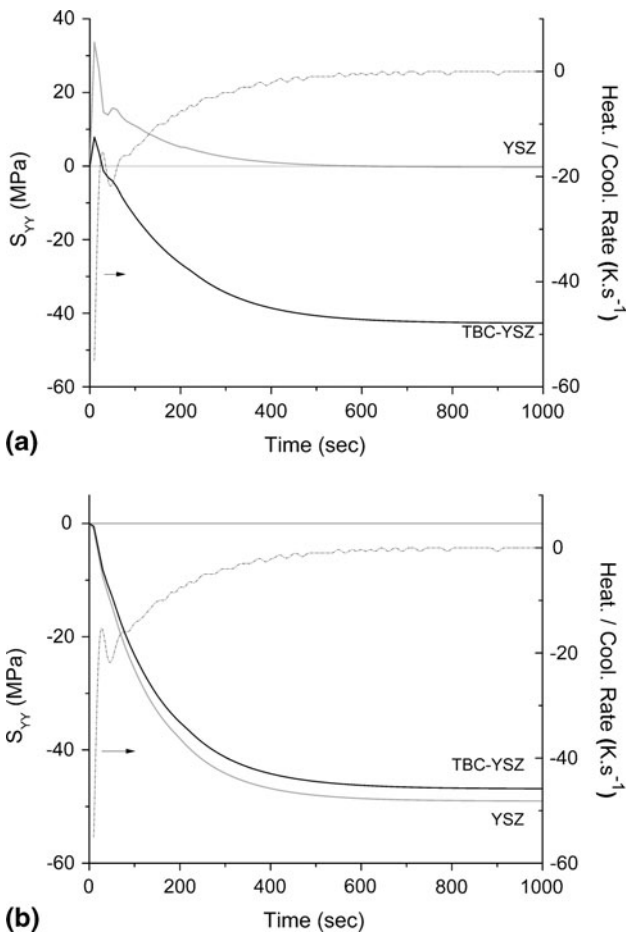


Fig. 4 Time-resolved in-plane normal stresses S_{YY} profiles for TBC-YSZ and YSZ samples during the post-deposition cooling step extracted from the metal/ceramic interface (a) and the ceramic's surface (b)

5.2 Thermal Cycle Step

The result of the calculated thermal cycle is presented in Fig. 5(b). Overall, it shows good agreement with the experimental record, Fig. 5(a). There is approximately a 2% difference between the calculated temperatures at the end of the heating period, and those measured. The maximum calculated temperature of the upper surface reaches 1318 K as against 1331 K in the furnace. On the lower face, the model predicts 988 K in comparison to 978 K under real conditions. The lowest calculated temperature achieved during the cycle, at the end of the cooling period, is 322 K as against 329 K noted in the experiment. The calculated heating rate during the first seconds is underestimated by 28% in comparison with the measured value in the quartz tube while the calculated cooling rate is closer to the measured value; the difference is of 6%. It can be reasonably assumed that the computed thermal down shock is well approximated by the finite element analysis. Globally, it can be concluded that the maximum and minimum temperatures, as well as the thermal up and down shocks, are well reproduced.

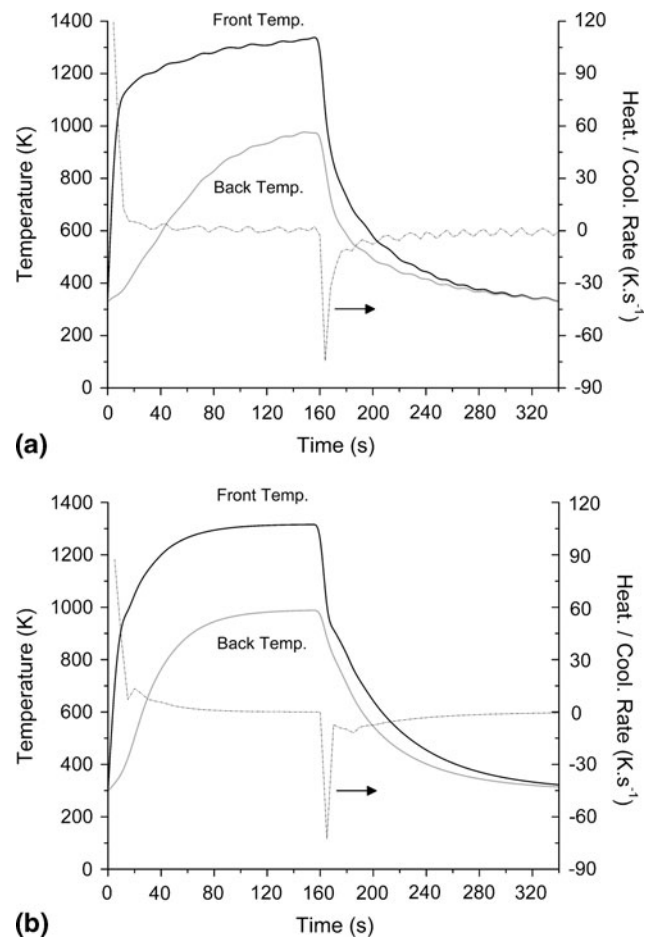
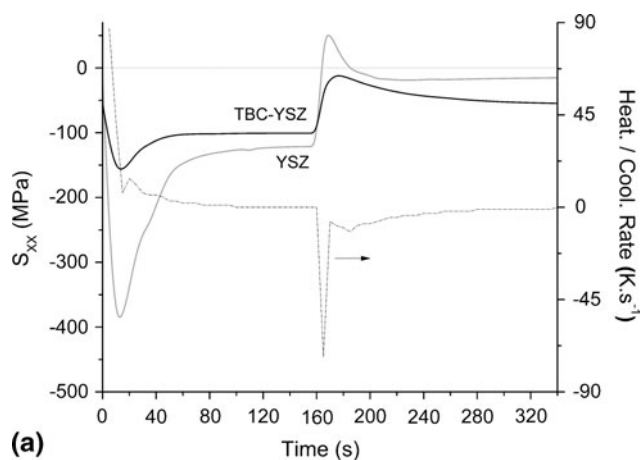


Fig. 5 Experimental (a), and calculated (b) temperature profiles and heating/cooling rates for, respectively, the front face and the back face of the TBC sample

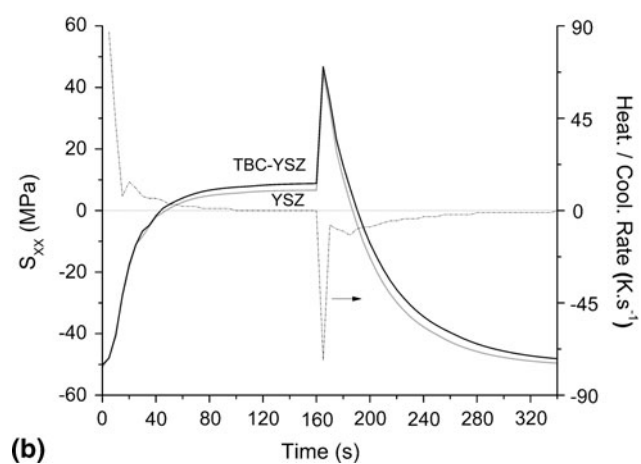
The development of in-plane normal stress according to time, during the cycle, is presented at the interface and at the surface of the ceramic layer, in the case of the YSZ and TBC-YSZ samples. In-plane S_{XX} normal stress is displayed in Fig. 6 while S_{YY} is shown in Fig. 7. The reference point is still the center of the barrier, at the mid-length and mid-width. The first stress state on the graph corresponds to the previous calculated stress state at the end of the post-deposition cooling step. Curves of the stress time development are characterized by different situations corresponding to the variations of the heating/cooling rate, also plotted on the curves using the second Y-axis to the right of the graph. The two zones, with important variations of the heating/cooling rates, correspond to the maximum stress intensity applied to the system, being either compressive during the up shock or tensile during the down shock. The up shock is characterized by the development of a strong compressive stress which effect is not being of interest for the reason that compressive stress is not supposed to propagate the pre-existing vertical cracks, arising from the release of the

quenching stress during the spraying step. Following the up shock, a zone with flat heating/cooling rates corresponds to slight variations of stresses with time. These stresses apply as a consequence of a non-homogeneous temperature throughout the sample's thickness, as shown in Fig. 5.

Globally during the heating step, the generated tensile stress shows increasing values from the interface to the surface of the ceramic layer. At the interface, tensile maxima are 13 MPa in case of YSZ sample, and 6 MPa in case of TBC-YSZ (Fig. 7a), while the upper part of the coating experienced tensile stresses up to 20-30 MPa, in both cases (Fig. 6b, 7b). No tensile stress arises along the X axis during this period (Fig. 6a). Maxima obtained for S_{XX} are in a general manner lower in both samples than the ones for S_{YY} . The tensile stress range occurred during the heating plateau is expected to contribute to the thermal aging of coatings, as well as during the post-deposition cooling step. The main difference between YSZ and TBC-YSZ samples, at the end of the heating period, is concentrated at the interface, where YSZ sample has

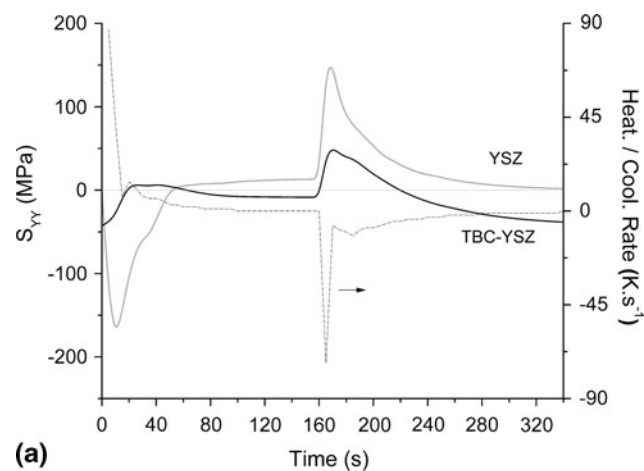


(a)

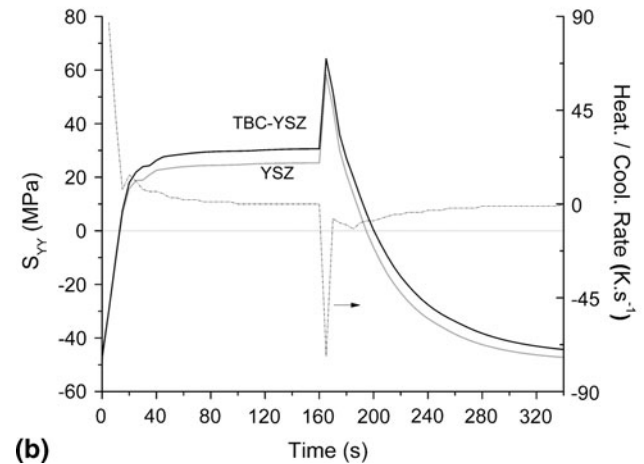


(b)

Fig. 6 Time-resolved in-plane normal stresses S_{XX} profiles for TBC-YSZ and YSZ samples during the thermal cycle, extracted from the metal/ceramic interface (a) and the ceramic's surface (b)



(a)



(b)

Fig. 7 Time-resolved in-plane normal stresses S_{YY} profiles for TBC-YSZ and YSZ samples during the thermal cycle, extracted from the metal/ceramic interface (a) and the ceramic's surface (b)

already sustained a higher stress range during the post-deposition cooling step that has modified the crack's length. Concerning the upper part of the ceramic layer, the stress range that had occurred until the end of the heating plateau is rather similar for both samples, and it can be concluded that the thermal aging of the samples within the upper part of the ceramic is still similar.

During the first seconds of the cooling step, i.e., around 20 s., the subsequent stress reaches the highest tensile values of the whole cycle, thus setting the highest stress range occurred since the end of spraying. Thus, the stress above the previous values, i.e., the one applying during the heating plateau, determines the contribution of the cycle's thermal down shock conditions to the degradation processes. In that way, and as a second remark about the model's results, it should be considered to discriminate AE counts corresponding to the heating period from those corresponding to the cooling period. The down shock is characterized by the development of a tensile stress in both samples. The maximum stress that is applied is in the order of 151 MPa for S_{YY} and 53 for S_{XX} in the case of YSZ sample, at the interface. In case of TBC-YSZ, the maximum stress at the interface is 50 for S_{YY} and S_{XX} remains compressive. At the surface, in-plane tensile stresses are in the same order for both samples, around 60 MPa for S_{YY} and 45 for S_{XX} . These values should be associated to the temperature gradient throughout the upper part of the ceramic layer. Following the down shock conditions, a second zone with flat heating/cooling rates takes place which corresponds to compressive stresses applied as a consequence of a homogeneous temperature throughout the sample's thickness, as shown in Fig. 5. Thus, it is concluded, after analyzing the results of the FE model, that different stress ranges have taken place, one during the post-deposition cooling step and the two others during the heating and the cooling period of cycle. Moreover, the stress range can be studied separately between the interface zone and the upper part of the ceramic layer.

6. Acoustic Emission Results

It has been proposed that the AE behavior is correlated to the stress intensity factor range ΔK , itself combining a stress range ΔS to a crack length. In a first step, short-term AE behavior monitoring has been performed for YSZ and TBC-YSZ. Results of the first cycle are displayed in Fig. 8. After the first thermal cycle, the TBC-YSZ sample has emitted a total of 66 AE against 45 in the case of the YSZ sample, showing a ratio of around 1.5. Nevertheless, it can be seen in Fig. 8 that the difference between both samples comes from the heating step, when the TBC-YSZ sample has emitted three times more AE than the YSZ sample. The FE analysis helps in interpreting that result. During the post-deposition cooling step, CTE mismatch according to thermal conditions has generated in-plane normal stresses in the order of 30 MPa at the interface in case of the YSZ sample. This stress has been distributed

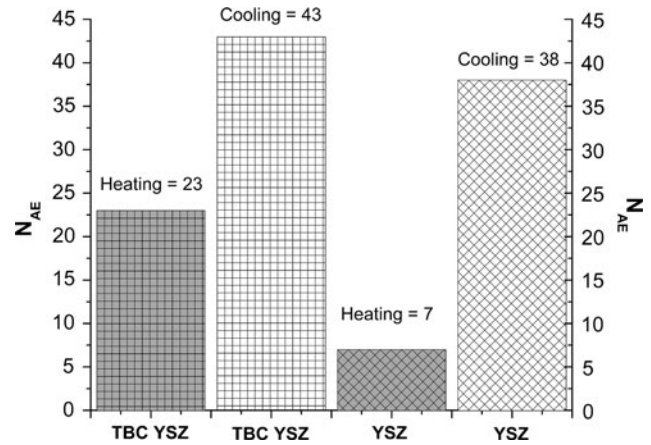


Fig. 8 Cumulative AE counts emitted during respectively the heating and cooling steps of the first thermal cycle, in case of respectively TBC-YSZ and YSZ samples

through the thickness of the sample, since the surface stress remains equal to zero and further decreases. Thus, YSZ and TBC-YSZ at the interface zone cannot be considered after the post-deposition cooling step as equivalent damaged structures. In the case of YSZ sample, the stress range that is applied during the post-deposition cooling step at the interface is higher than the one that is applied during the heating period, limiting the increase of the stress intensity factor. The upper part of the ceramic layer shows the application of similar stress range in both samples. Thus, since triggering more AE is supposed to have a higher stress intensity factor, it is expected that less AE counts are observed during the first heating period for the YSZ sample than for the TBC-YSZ sample. With reasonable confidence, it can be considered that the actual AE behavior of the two samples confirms that point. The model shows that during thermal loading, the highest stress range occurs during the cooling step of the cycle. During the first seconds of the cooling, the FE model points out that TBC-YSZ and YSZ show similar stress range in the upper part of the ceramic layer. The lack of bond coat in case of YSZ sample induces a higher stress range at the ceramic/metal interface than during the cooling step. Therefore both samples are expected to sustain a substantial increase in the stress intensity factor range and produce a corresponding substantial amount of AE. Also in that case the actual AE behavior of the samples confirms this point.

The actual AE behavior of the samples allows thinking that the crack growth rate during the heating period is lower in the case of YSZ sample than in the case of TBC-YSZ sample. The only way to explain that point is to consider longer "apparent" cracks lengths, i.e., a more advanced thermal aging, within the YSZ sample than within the TBC-YSZ sample. The latter can be explained by the occurrence of a higher stress range during the post-deposition cooling step, resulting in a higher crack growth. Thus, one who wants to use the cumulative number of AE as a phenomenological damage variable

should start the monitoring from the spraying step. In case of the stress intensity factor range used as the phenomenological damage variable, its determination should take place also during the spraying. If it is not the case, then the setting up of a parameter based on the AE count is needed. It is proposed to calculate the ratio of the AE number occurring during the cooling period over the AE number during the heating period. By this way, the acoustic ratio, R , so obtained is considered to be proportional to the highest stress intensity factor range that had occurred since spraying, and had set the ultimate crack length. Such a variable is considered to be a phenomenological damage variable representing the thermal aging of the investigated sample. This variable should be fitted by a power-law similar to the one of the Basquin's model to assess the remaining fatigue life of the structure submitted to a defined cycling thermal load.

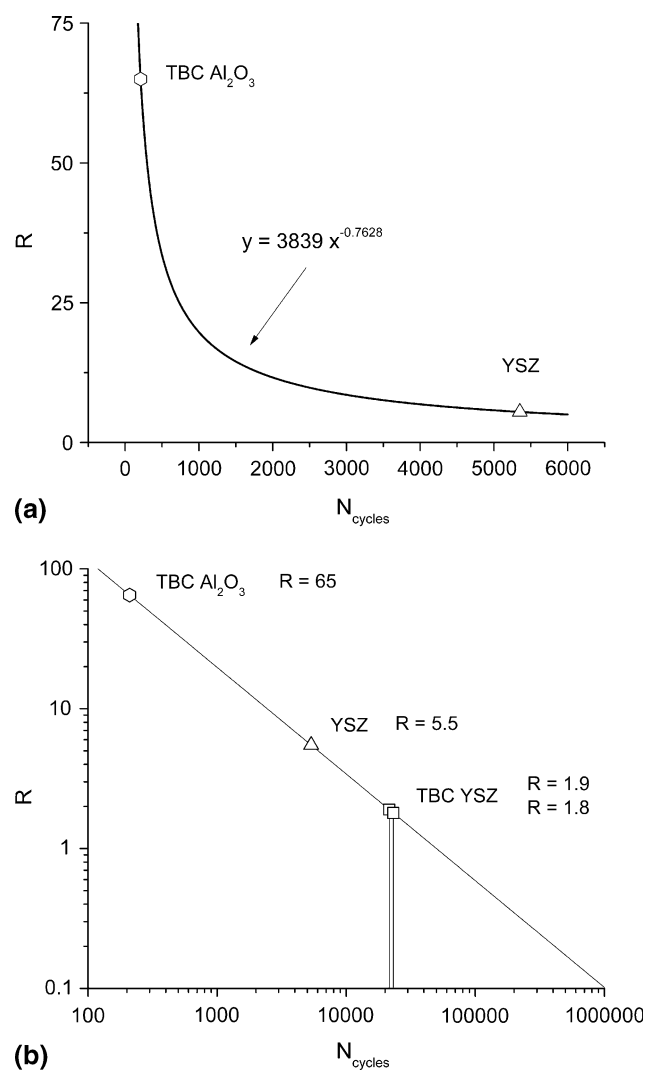


Fig. 9 Power-law fitting of the acoustic parameter, R , as described (a) and the graphic resolution of the predicted performance for the two TBC-YSZ samples (b)

TBC- Al_2O_3 has been qualified in this study as a known material to have a poor thermal shock resistance. Moreover, its resistance is lowered by phase transformations that occur during temperature changes over 900-1000 °C. Thus, the thermal aging of the TBC Al_2O_3 sample is expected to be the fastest of all samples. During thermal cycling test, the TBC- Al_2O_3 sample showed the lowest number of cycles to failure i.e., 210 cycles. It showed also the highest acoustic ratio, in the order of 65. Following TBC- Al_2O_3 , the YSZ sample failed at 5350 cycles showing an acoustic ratio of 5.5. These values are plotted versus the numbers of cycles to failure in case of the TBC Al_2O_3 and YSZ samples. The curve so obtained is presented in Fig. 9(a), as well as the power-law fitting.

Two TBC-YSZ samples have been subjected to the first cycle tests, showing very close acoustic ratio values, 1.8 and 1.9. The graphic resolution of the predicted performance under the defined cyclic thermal load of the two TBC-YSZ samples is displayed in Fig. 9(b). Following the proposed model, TBC-YSZ samples are expected to sustain more than 2×10^4 cycles. Such a test has been conducted, i.e., the long-term monitoring of the AE behavior has been performed, and, after more than 2×10^4 cycles, ceramic coatings show thermal aging, i.e., numerous micro-cracks, but not any evidence of spallation or macroscopic defect. The long-term AE behavior monitoring is presented elsewhere (Ref 6). Thus, it can be concluded that the TBC-YSZ sample has passed the test and that the acoustic parameter shows a reasonable agreement with a phenomenological variable that characterizes the thermomechanical damages induced by the first thermal cycling of a precracked sample.

7. Conclusion

It should ever be considered to separate the AE behavior monitoring during the heating and cooling periods of a thermal cycle. These periods show different stress ranges that correspond to different crack lengths and, therefore, correspond to different stress intensity factor ranges. The FEM has been helpful in determining the stress range that has triggered the AE behavior of the YSZ and TBC-YSZ samples. Then, the AE behavior during the heating and cooling periods of the first cycle has been helpful in estimating the stress intensity factor range. Finally, the acoustic parameter, R , shows a reasonable good agreement with the remaining cyclic fatigue cyclic life and, thus, is the phenomenological damage variable to be considered at the end of the first cycle. It shows potential in determining the remaining fatigue life in terms of pure thermal cycles, i.e., the isothermal time is limited to the minimum, and could be used in a large range of applications. For example, it could be used to set the highest temperature drop within a cycle that corresponds to an adjusted acoustic ratio. As a final remark, the AE behavior will depend on the ratio of the ceramic coating volume over the interface area, with all other parameters being equal. In the case of square samples, this

ratio is reduced to the thickness of the ceramic layer. For more developed structures, it should be considered important to evaluate this value to compare or transfer the results.

References

1. A.G. Evans, D.R. Mumm, J.W. Hutchinson, G.H. Meier, and F.S. Pettit, Mechanisms Controlling the Durability of Thermal Barrier Coatings, *Prog. Mater. Sci.*, 2001, **46**, p 505-553
2. A.G. Evans and J.W. Hutchinson, The Mechanics of Coating Delamination in Thermal Gradients, *Surf. Coat. Technol.*, 2007, **201**(18), p 7905-7916
3. C.C. Berndt, Acoustic Emission Evaluation of Plasma-Sprayed Thermal Barrier Coatings, *J. Eng. Gas Turbines Power*, 1985, **107**, p 142-146
4. C.C. Berndt, C.K. Lin, and S.H. Leigh, Characterization of Cracking within Thermal Spray Deposits by an Acoustic Emission Method, *J. Therm. Spray Technol.*, 1998, **7**(3), p 334-336
5. N.R. Shankar, C.C. Berndt, H. Herman, and S. Rangaswamy, Acoustic Emission from Thermally Cycled Plasma Sprayed Oxides, *Am. Ceram. Soc. Bull.*, 1983, **62**(5), p 614-619
6. P.C. Robin, F. Gitzhofer, P.L. Fauchais, and M.I. Boulos, Lamb Waves Monitoring of the Thermomechanical Aging Effects in Ceramic Coatings, *Surf. Coat. Technol.*, 2007, **201**(18), p 7764-7774
7. Z. Gan, H.W. Ng, and A. Devasenapathi, Deposition-Induced Residual Stresses in Plasma-Sprayed Coatings, *Surf. Coat. Technol.*, 2004, **187**(2-3), p 307-319
8. M. Wenzelburger, M. Escribano, and R. Gadow, Modeling of Thermally Sprayed Coatings on Light Metal Substrates: Layer Growth and Residual Stress Formation, *Surf. Coat. Technol.*, 2004, **180-181**, p 429-435
9. V. Moorthy, T. Jayakumar, and B. Raj, Acoustic Emission Behaviour During Stage II, Fatigue Crack Growth in an AISI, Type 316 Austenitic Stainless Steel, *Bull. Mater. Sci.*, 1994, **17**(6), p 699-715
10. D. Fargeot, D. Mercurio, and A. Dager, Structural Characterization of Alumina Metastable Phase in Plasma Sprayed Deposits, *Mater. Chem. Phys.*, 1990, **24**, p 299-314
11. R. Krishnan, S. Dash, R. Kesavamoorthy, C. Babu Rao, A.K. Tyagi, and B. Raj, Laser Surface Modification and Characterization of Air Plasma Sprayed Alumina Coatings, *Surf. Coat. Technol.*, 2006, **200**, p 2791-2799
12. R.J. Damani and E.H. Lutz, Microstructure, Strength and Fracture Characteristics of a Free-Standing Plasma-Sprayed Alumina, *J. Eur. Ceram. Soc.*, 1997, **17**, p 1351-1359
13. R.J. Damani and P. Makroczy, Heat Treatment Induced Phase and Microstructural Development in Bulk Plasma Sprayed Alumina, *J. Eur. Ceram. Soc.*, 2000, **20**(7), p 867-888
14. S. Kuroda and T.W. Clyne, Quenching Stress in Thermally Sprayed Coatings, *Thin Solid Films*, 1991, **200**, p 49-66
15. L. Bianchi, A.C. Leger, M. Vardelle, A. Vardelle, and P. Fauchais, Splat Formation and Cooling of Plasma Sprayed Zirconia, *Thin Solid Films*, 1997, **305**, p 35-48
16. Y. Liu, C. Persson, and S. Melin, Numerical Modeling of Short Crack Behavior in a Thermal Barrier Coating upon Thermal Shock Loading, *J. Therm. Spray Technol.*, 2004, **13**, p 554-560
17. A. Wöhler, Über die festigkeits-versuche mit eisen und stahl, *Zeitschrift für Bauwesen*, 1870, **20**, p 73-106
18. W. Schütz, A History of Fatigue, *Eng. Fract. Mech.*, 1996, **54**(2), p 263-300
19. T.M. Roberts and M. Talebzadeh, Fatigue life Prediction Based on Crack Propagation and Acoustic Emission Count Rates, *Constr. Steel Res.*, 2003, **59**(6), p 679-694
20. P.C. Paris and F. Erdogan, A Critical Analysis of Crack Propagation Laws, *J. Basic Eng.*, 1963, **85**, p 528-534
21. R.S. Li and A. Chudnovsky, Examination of the Fatigue Crack Growth Equations, *Int. J. Fract.*, 1996, **81**(4), p 343-355
22. T.M. Roberts and M. Talebzadeh, Acoustic Emission Monitoring of Fatigue Crack Propagation, *Constr. Steel Res.*, 2003, **59**(6), p 695-712
23. Z. Gong, E.O. Nyborg, and G. Oommen, Acoustic Emission Monitoring of Steel Railroad Bridges, *Mater. Eval.*, 1992, **50**, p 883-887
24. F.P. Incropera and D.P. DeWitt, *Fundamentals of Heat and Mass Transfer*, 5th ed., John Wiley & Sons, New York, 2001, p 981
25. R.J. Damani and A. Wanner, Microstructure and Elastic Properties of Plasma-Sprayed Alumina, *J. Mater. Sci.*, 2000, **35**, p 4307-4318
26. L. Pawlowski, *The Science and Engineering of Thermal Spray Coatings*, John Wiley & Sons, New York, 1995, p 414
27. Y.S. Touloukian, *Thermophysical Properties of Matter [The TPRC Data Series, a Comprehensive Compilation of Data]*, 12 Volumes, IFI/Plenum Press, New York, 1976
28. D.R. Mumm and A.G. Evans, Mechanisms controlling the Performance and Durability of Thermal Barrier Coatings, *Key Eng. Mater.*, 2001, **197**, p 199-230
29. D.L. Vasquez, A. Kucuk, R.S. Lima, U. Senturk, and C.C. Berndt, Elastic Modulus Measurements of Air Plasma Sprayed Yttria Partially Stabilized Zirconia Coatings Using Laser Ultrasonics and Indentation Techniques, *Thermal Spray 2003: Advancing the Science and Applying the Technology*, B.R. Marple and C. Moreau, Ed., May 5-8, 2003 (Orlando, FL), ASM International, 2003, p 1045-1050
30. P. Robin, "Modelisation et Diagnostic de Barrières Thermiques sous Chargement Thermique Cyclique" (Modeling and Diagnostic of Thermal Barrier Coatings under Thermal Cycling Load), Ph.D. thesis, Université de Sherbrooke/Université de Limoges, 2005, 274 p (In French)
31. P.C. Robin, F. Gitzhofer, M.I. Boulos, P.L. Fauchais, and M. Hogge, Finite Elements Modelling of Transient Thermal Stresses Developed in Ceramic Coatings During Thermal Cycling Conditions, *Thermal Spray 2005: Thermal Spray connects: Explore Its Surfacing Potential!*, E. Lugscheider, Ed., May 2-4, 2005 (Basel, Switzerland), DVS-Verlag, 2005, p 265-270